Colloid Polym Sci (2004) 282: 620–632
DOI 10.1007/s00396-003-0987-x

ORIGINAL CONTRIBUTION

Frederico W. Tavares
John M. Prausnitz

Analytic calculation of phase diagrams for solutions containing colloids or globular proteins

Received: 19 May 2003
Accepted: 20 August 2003

F. W. Tavares · J. M. Prausnitz (✉)
Department of Chemical Engineering,
University of California, Berkeley,
CA 94720-1462, USA
E-mail: prausnit@cchem.berkeley.edu

J. M. Prausnitz
Chemical Sciences Division,
Lawrence Berkeley National Laboratory,
Berkeley, CA 94720, USA

F. W. Tavares
Escola de Química, Universidade Federal
do Rio de Janeiro, Caixa Postal 68542,
CEP 21949-900 Rio de Janeiro, RJ, Brazil

Abstract Second-order Barker–Henderson perturbation theory gives phase diagrams for colloid and protein solutions that include stable and metastable fluid–fluid, solid–fluid, and solid–solid phases. The potential of mean force is described by a hard-sphere interacting with a Yukawa potential. Calculations for different ranges of attraction show that, as expected, fluid–fluid coexistence becomes metastable when the potential becomes short-ranged. For a very short-ranged Yukawa potential, the phase diagram shows isostructural solid–solid equilibria with a critical point. To test more simplified models, phase diagrams from second-order Barker–Henderson perturbation theory are compared with those from the random-phase approximation for the fluid phase and the van der Waals theory for the solid phase; this comparison shows significantly different phase diagrams. Moreover, with a potential of mean force with primary and secondary minima, calculations using second-order perturbation theory identify conditions where colloidal and protein solutions can present two fluid–fluid regions, each with a critical point; however, the higher-density fluid–fluid region is likely to be metastable. The analytic calculations described here may be useful for interpretation of experimental phase diagrams and for guiding design of separation processes.

Keywords Colloidal stability
Protein precipitation · Phase diagrams · Solid–fluid equilibrium
Statistical thermodynamics

Introduction

The phase behavior of colloidal solutions is of interest in a variety of technical applications, including paints, inks, coatings, and high-tech materials for optical, structural, and medical purposes. Because solutions of globular proteins are similar to colloidal solutions, the phase behavior of colloidal solutions is also of direct interest in biotechnology [1].

Anderson and Lekkerkerker [2] have indicated that colloids display intriguing phase transitions between fluid–fluid, fluid–solid, and solid–solid phases. In colloid and protein systems, stable phase equilibria are not always achieved because these systems often become trapped in a metastable condition as undercooled, supersaturated, or gel-like states.

Liquids and their mixtures can often exist for a long time under metastable conditions [3]. The existence of a metastable region in a phase diagram may be important because it influences the rate of phase transformations, for example., crystallization [2, 4, 5]. Therefore, toward better understanding of the mechanisms of phase transitions for colloid and protein systems, it is useful to describe a complete phase diagram that shows not only the domains of stable phases but also those of metastable states.

The literature is rich with articles [2, 3, 4, 5, 6, 7, 8, 9, 10, 11, 12, 13, 14] discussing phase diagrams of colloidal and similar solutions; here, a phase diagram is a plot of temperature against the concentration of colloidal particles, often called density. Most of these articles describe results obtained from molecular simulations. However, for applications, especially for optimization in product and process design, it is preferable to obtain results for a variety of conditions; in that event, results from molecular simulations are not as useful as those obtained from analytic methods. Therefore, in this work we present an overview of such methods. For comparison, we present results based on analytic approximations and we compare our analytic results with those obtained by molecular simulation. Consistent with numerous reports in the literature, we show once again that the phase diagram is sensitive to the attractive range of the potential of mean force for describing colloid–colloid (or protein–protein) interactions in solution.

Long-range attractive interactions between two molecules have a strong influence on vapor–liquid (or fluid–fluid) equilibria. As shown by numerous authors, the range of the attractive interaction affects the stability of the fluid–fluid transition [6, 7, 8, 9, 10, 11, 12, 13, 14]. When the interaction potential becomes short-ranged, the stable fluid–fluid phase transition disappears and only the solid–fluid coexistence curve is thermodynamically stable. As pointed out by Dijkstra [14], the range of attraction in the potential cannot be changed for ordinary fluids, but it can be adjusted in aqueous protein systems by adding, for example, a nonadsorbing polymer or ions. As shown by simulation studies, the minimum range of the attraction required for stable fluid–fluid coexistence is about one sixth of the particle diameter. For very short-ranged attractions, smaller than about 1/20th of the particle diameter, a stable isostructural solid–solid transition appears [14, 15].

In this work, we present analytic thermodynamic calculations for obtaining a complete phase diagram, including metastable coexistence regions. These calculations hold for ordinary fluids and for colloid and globular protein solutions. Attention here is restricted to spherical particles.

Our potential of mean force, φ, is for a perturbed hard sphere with diameter σ, with a perturbation attractive part: $\varphi=\infty$ for $r<\sigma$ and $\varphi=u^{\mathrm{P}}$ for $r\geq\sigma$, where r is the center-to-center distance and u^{P} is the perturbation potential. We compare results from second-order Barker–Henderson perturbation theory with those from simpler models: the random-phase approximation (RPA) for fluids and the van der Waals theory for solids. We use the attractive Yukawa function for the perturbation potential. Because of its flexibility, the Yukawa potential has been applied previously to describe a variety of fluids: electrolytes, molten salts, liquid metals, dense plasmas, colloidal dispersions, micelles, and microemulsions. Upon varying the range of the interaction in the Yukawa model, we can reproduce the behavior of real systems. We compare our results with those from recent molecular-simulation data [16].

We have also explored the possibility that a colloid and protein solution may present two fluid–fluid critical points, one at low density and the other at high density. A first-order transition between two high-density liquids seems to be consistent with recent experimental data for water [17], phosphorus [18], silica [19] and carbon [20]. According to Hemmer et al. [21], Franzese et al. [22], and Malescio et al. [23], phase diagrams with two critical points exist for fluids that interact with a second repulsion potential, i.e., a potential with an attractive part and with two characteristic ranges of repulsive interaction (either soft or hard). We consider whether a colloid system can exhibit more than one fluid–fluid critical point. For this calculation we used a potential of mean force containing two minima.

Theoretical framework

We obtain thermodynamic properties and phase diagrams using perturbation theories applied to both fluid and solid phases. The potential of mean force is given by a hard sphere with a perturbation potential. The total Helmholtz energy of the system, A, is a sum of the hard-sphere and perturbation contributions:

$$\frac{A}{Nk_{\mathrm{B}}T}=\frac{A^{\mathrm{HS}}}{Nk_{\mathrm{B}}T}+\frac{A^{\mathrm{P}}}{Nk_{\mathrm{B}}T}, \tag{1}$$

where A^{HS} is the total Helmholtz energy for the hard-sphere fluid (reference system) and A^{P} is the perturbation contribution. N is the number of molecules, k_{B} is the Boltzmann constant, and T is the temperature. The equation of state is obtained by differentiating the Helmholtz energy with respect to the packing fraction η:

$$Z=\eta\left(\frac{\partial\left(\frac{A}{Nk_{\mathrm{B}}T}\right)}{\partial\eta}\right)=Z^{\mathrm{HS}}+Z^{\mathrm{P}}, \tag{2}$$

where $Z=p/(\rho k_{\mathrm{B}}T)$ is the compressibility factor of the system, p is the pressure, and ρ is the density. The packing fraction is defined as $\eta=(\pi\rho\sigma^3)/6$, and $\rho\sigma^3$ is the reduced density. Z^{HS} and Z^{P} are compressibility-factor contributions, one from the hard-sphere term and the other from the perturbation. The chemical potential of the system, μ, is obtained by

$$\frac{\mu}{k_{\mathrm{B}}T}=\frac{A}{Nk_{\mathrm{B}}T}+Z=\frac{\mu^{\mathrm{HS}}}{k_{\mathrm{B}}T}+\frac{\mu^{\mathrm{P}}}{k_{\mathrm{B}}T}, \tag{3}$$

where μ^{HS} and μ^{P} are, respectively, the hard-sphere and perturbation contributions. For the hard-sphere contribution, we use the Carnahan–Starling equation for the fluid and the model of Velasco et al. [24] for the solid.

We use three statistical-thermodynamic models to calculate the perturbation contribution to the Helmholtz energy for the fluid: the RPA and the first-order and second-order Barker–Henderson perturbation theories. For the perturbation contribution to the Helmholtz energy for a solid we use the van der Waals theory (for solids), and the first-order or second-order Barker–Henderson perturbation theories. These models are presented in the next two sections.

For calculating the phase diagram at a fixed temperature, we use the conventional equations for phase equilibria:

$$\mu = \mu, \tag{4}$$

$$p = p, \tag{5}$$

where superscripts ′ and ″ refer to phases.

In the isothermal equations for phase equilibria, μ and p are functions of density (or packing fraction). There are two unknowns: the density of phase ′ and the density of phase ″. These densities of the coexisting phases are obtained by simultaneous solution of Eqs. (4) and (5).

To obtain the necessary expressions for μ and p as a function of temperature and density, we need two separate theories, one for the fluid and the one for the solid; these are described here. However, in addition we need information on intermolecular forces as expressed thorough a potential function. For colloids and globular proteins in a solvent, the necessary potential function is the potential of mean force, i.e., the potential of two particles in a continuous medium that represents the solvent. We use the same potential of mean force for all phases, liquid and solid.

Equations for thermodynamic properties of the fluid phase

The Carnahan–Starling equation of state provides the hard-sphere contribution. The Helmholtz energy is

$$\frac{A^{\mathrm{HS}}}{Nk_{\mathrm{B}}T} = \ln\left(\frac{6\Lambda^3\eta}{\pi\sigma^3}\right) - 1 + \frac{4\eta - 3\eta^2}{(1-\eta)^2}. \tag{6}$$

The first two terms on the right side of Eq. (6) comprise the Helmholtz energy of an ideal gas, where Λ is the thermal de Broglie wavelength. The last term is the hard-sphere residual contribution. The Carnahan–Starling equation of state is

$$Z^{\mathrm{HS}} = \frac{1 + \eta + \eta^2 - \eta^3}{(1-\eta)^3}. \tag{7}$$

The chemical potential of the hard-sphere system, μ^{HS}, is obtained from

$$\begin{aligned}\frac{\mu^{\mathrm{HS}}}{k_{\mathrm{B}}T} &= \frac{A^{\mathrm{HS}}}{Nk_{\mathrm{B}}T} + Z^{\mathrm{HS}}\\ &= \ln\left(\frac{6\Lambda^3\eta}{\pi\sigma^3}\right) - 1 + \frac{4\eta - 3\eta^2}{(1-\eta)^2} + \frac{1 + \eta + \eta^2 - \eta^3}{(1-\eta)^3}.\end{aligned} \tag{8}$$

The first two terms on the right side of Eq. (8) give the chemical potential of an ideal gas.

RPA for the fluid

The RPA is, essentially, a first-order perturbation theory where the perturbation is given by the van der Waals approximation [25], which assumes that the probability of finding a molecule around a central molecule is directly proportional to the number density, independent of the distance from the central molecule. In this approximation, the fluid has no structure because, by assumption, the radial distribution function (RDF) is constant, independent of temperature and density. Using the RPA, the perturbation contributions to the Helmholtz energy, compressibility factor, and chemical potential are

$$\left(\frac{A^{\mathrm{P}}}{Nk_{\mathrm{B}}T}\right)^{\mathrm{RPA}} = \frac{12\eta}{T^*}\int_1^\infty u^{\mathrm{P}*}s^2\mathrm{d}s, \tag{9}$$

$$\left(Z^{\mathrm{P}}\right)^{\mathrm{RPA}} = \frac{12\eta}{T^*}\int_1^\infty u^{\mathrm{P}*}s^2\mathrm{d}s, \tag{10}$$

$$\left(\frac{\mu^{\mathrm{P}}}{k_{\mathrm{B}}T}\right)^{\mathrm{RPA}} = \frac{24\eta}{T^*}\int_1^\infty u^{\mathrm{P}*}s^2\mathrm{d}s. \tag{11}$$

The reduced temperature is $T^* = k_{\mathrm{B}}T/\varepsilon$, where ε is the energy parameter of the potential, and $u^{\mathrm{P}*} = u^{\mathrm{P}}/\varepsilon$ is the reduced perturbation potential; it is a function of the reduced distance between two particles, $s = r/\sigma$, where r is the center-to-center distance of separation between to particles. In the RPA, the integral $\int_1^\infty u^{\mathrm{P}*}s^2\mathrm{d}s$ is constant, independent of temperature and density. Therefore, the perturbation contributions to the Helmholtz energy, $(A^{\mathrm{P}})^{\mathrm{RPA}}$, the equation of state, $(Z^{\mathrm{P}})^{\mathrm{RPA}}$, and the chemical potential, $(\mu^{\mathrm{P}})^{\mathrm{RPA}}$, are analytic expressions. The remarkably simple expressions provided by the RPA make it attractive for application to engineering problems but, as shown later, there is a serious disagreement between results from the RPA and those from molecular simulation.

Barker–Henderson perturbation theory for a fluid

The first-order and second-order Barker–Henderson perturbation theories are described by McQuarrie [25].

As pointed out by Boublik et al. [26], in the second-order theory, the local compressibility approximation provides better accuracy than the macroscopic compressibility approximation. Using the local compressibility approximation, the perturbation contribution to the Helmholtz energy is [25]

$$\left(\frac{A^{\mathrm{P}}}{Nk_{\mathrm{B}}T}\right)^{\mathrm{BH}} = \frac{12\eta}{T^*}\int_1^\infty u^{\mathrm{P}*}g^{\mathrm{HS}}s^2\mathrm{d}s - \frac{6\eta}{(T^*)^2\left(\frac{\partial(p/k_{\mathrm{B}}T)}{\partial\rho}\right)^{\mathrm{HS}}}\int_1^\infty \left(u^{\mathrm{P}*}\right)^2\left(g^{\mathrm{HS}} + \eta\frac{\partial g^{\mathrm{HS}}}{\partial\eta}\right)s^2\mathrm{d}s \tag{12}$$

We refer to first-order perturbation when the second term on the right side in Eq. (12) is neglected, and to second-order perturbation when both terms in Eq. (12) are used. Inside the integrals, g^{HS} is the RDF of the hard-sphere fluid. This function depends on packing fraction η and reduced distance s.

Although the Carnahan–Starling equation of state is used to calculate the Helmholtz energy and the compressibility factor of the hard-sphere reference system (Eqs. 6, 7), we follow the original suggestion of Barker and Henderson and use the Percus–Yevick compressibility expression [25] for $\left(\frac{\partial(p/k_{\mathrm{B}}T)}{\partial\rho}\right)^{\mathrm{HS}}$ in the second-order term of the perturbation expansion. Using the Percus–Yevick compressibility equation of state, the perturbation contributions to the Helmholtz energy, the equation of state, and the chemical potential are

$$\left(\frac{A^{\mathrm{P}}}{Nk_{\mathrm{B}}T}\right)^{\mathrm{BH}} = \frac{12\eta\mathbf{I}_1}{T^*} - \frac{6\eta(1-\eta)^4}{(1+4\eta+4\eta^2)}\left(\mathbf{I}_2 + \eta\frac{\partial\mathbf{I}_2}{\partial\eta}\right)\frac{1}{(T^*)^2}, \tag{13}$$

$$\begin{aligned}\left(Z^{\mathrm{P}}\right)^{\mathrm{BH}} = {} & \frac{12\eta}{T^*}\left(\mathbf{I}_1 + \eta\frac{\partial\mathbf{I}_1}{\partial\eta}\right) \\ & - \frac{6\eta^2(1-\eta)^4}{(1+4\eta+4\eta^2)}\left(\mathbf{I}_2 + 3\eta\frac{\partial\mathbf{I}_2}{\partial\eta} + \eta^2\frac{\partial^2\mathbf{I}_2}{\partial\eta^2}\right)\frac{1}{(T^*)^2} \\ & - \frac{6\eta(1-\eta)^3\left(1-5\eta-20\eta^2-12\eta^3\right)}{(1+4\eta+4\eta^2)^2} \\ & \times\left(\mathbf{I}_2 + \eta\frac{\partial\mathbf{I}_2}{\partial\eta}\right)\frac{1}{(T^*)^2},\end{aligned} \tag{14}$$

and

$$\begin{aligned}\left(\frac{\mu^{\mathrm{P}}}{k_{\mathrm{B}}T}\right)^{\mathrm{BH}} = {} & \frac{12\eta}{T^*}\left(2\mathbf{I}_1 + \eta\frac{\partial\mathbf{I}_1}{\partial\eta}\right) \\ & - \frac{6\eta^2(1-\eta)^4}{(1+4\eta+4\eta^2)}\left(2\mathbf{I}_2 + 4\eta\frac{\partial\mathbf{I}_2}{\partial\eta} + \eta^2\frac{\partial^2\mathbf{I}_2}{\partial\eta^2}\right) \\ & \times\frac{1}{(T^*)^2} - \frac{6\eta(1-\eta)^3\left(1-5\eta-20\eta^2-12\eta^3\right)}{(1+4\eta+4\eta^2)^2} \\ & \times\left(\mathbf{I}_2 + \eta\frac{\partial\mathbf{I}_2}{\partial\eta}\right)\frac{1}{(T^*)^2},\end{aligned} \tag{15}$$

where the integrals are

$$\begin{aligned}\mathbf{I}_1 &= \int_1^{s_{\max}} u^{\mathrm{P}*}g^{\mathrm{HS}}s^2\mathrm{d}s, \\ \frac{\partial\mathbf{I}_1}{\partial\eta} &= \int_1^{s_{\max}} u^{\mathrm{P}*}\left(\frac{\partial g^{\mathrm{HS}}}{\partial\eta}\right)s^2\mathrm{d}s, \\ \mathbf{I}_2 &= \int_1^{s_{\max}} \left(u^{\mathrm{P}*}\right)^2 g^{\mathrm{HS}}s^2\mathrm{d}s, \\ \frac{\partial\mathbf{I}_2}{\partial\eta} &= \int_1^{s_{\max}} \left(u^{\mathrm{P}*}\right)^2\left(\frac{\partial g^{\mathrm{HS}}}{\partial\eta}\right)s^2\mathrm{d}s, \\ \frac{\partial^2\mathbf{I}_2}{\partial\eta^2} &= \int_1^{s_{\max}} \left(u^{\mathrm{P}*}\right)^2\left(\frac{\partial^2 g^{\mathrm{HS}}}{\partial\eta^2}\right)s^2\mathrm{d}s.\end{aligned} \tag{16}$$

Here, $s_{\max}$ is the maximum reduced distance where the integrals in Eq. (16) are evaluated. The RDF g^{HS} for a hard-sphere fluid, calculated from equations given by Chang and Sandler [27], is shown in Fig. 1. Figure 1 shows that a rise in the packing fraction produces an increase in the probability of finding a molecule at contact with a central molecule.

Equations for thermodynamic properties of the solid phase

For the solid phase, either one of two equations of state is used for comparison. The first is based on the van der Waals theory for a solid [9] and the second is based on second-order Barker–Henderson perturbation theory similar to that described elsewhere [7, 13].

A simple expression for the Helmholtz energy for a hard-sphere solid was suggested by Velasco et al. [24] and discussed by Wu and Prausnitz [9] (also J.Z. Wu, 2002, personal communication). As pointed out by Wu and Prausnitz [9], the original cell model implicitly assumes impenetrable walls between neighboring particles.

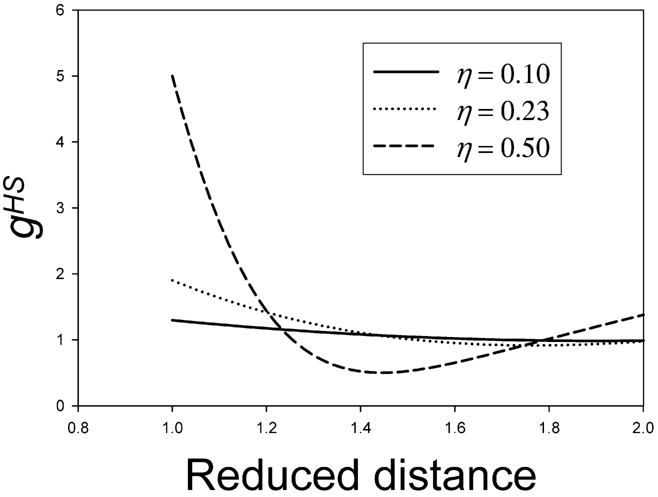

Fig. 1 Radial distribution function for a hard-sphere fluid at three different packing fractions calculated from equations given by Chang and Sandler [27]

While this assumption is convenient for deriving the partition function, the presence of cell walls incorrectly limits the freedom of individual particles; in a real solid, particle confinement is not due to the fictitious cell walls but to interparticle repulsion. As long as there is no overlap with its neighbors, each particle is allowed to move across its cell boundary, i.e., the displacement length for each particle should be twice that of the original cell model. Based on the Wigner–Seitz cell model for a hard-sphere solid, Velasco and coworkers derived expressions for the Helmholtz energy and for the corresponding equation of state that include these extended translational degrees of freedom:

$$\frac{A^{\mathrm{HS}}}{Nk_{\mathrm{B}}T} = \ln\left(\frac{6\Lambda^3\eta}{\pi\sigma^3}\right) - 3\ln\left[1-(\eta/\eta_0)^{1/3}\right] - 3\ln 2 \qquad (17)$$

and

$$Z^{\mathrm{HS}} = \frac{1}{\left[1-(\eta/\eta_0)^{1/3}\right]}. \qquad (18)$$

The chemical potential for a hard-sphere solid is

$$\frac{\mu^{\mathrm{HS}}}{k_{\mathrm{B}}T} = \ln\left(\frac{6\Lambda^3\eta}{\pi\sigma^3}\right) - 3\ln\left[1-(\eta/\eta_0)^{1/3}\right] - 3\ln 2 + \frac{1}{\left[1-(\eta/\eta_0)^{1/3}\right]}, \qquad (19)$$

where $\eta_0 = \pi\sqrt{2}/6$ is the maximum packing fraction for a crystal within a face-centered-cubic (fcc) structure. The first term on the right side in Eq. (17) represents the ideal-gas (confined in the lattice) limit. When fluid–solid equilibria are calculated using Eqs. (18) and (19) (using the Carnahan–Starling equation of state to describe the fluid phase), the results are consistent with the simulation data of Hoover and Ree [28]. As pointed out by Wu (personal communication), the modified cell model gives freezing and melting packing fractions equal to 0.492 and 0.555, respectively, in close agreement with molecular-simulation results (0.494 and 0.545). We have obtained the same results, confirming Wus observation.

van der Waals theory for a solid

The van der Waals theory for a solid is a first-order perturbation with a simplified RDF. According to this theory, the probability of finding a neighboring particle is given by a δ function that is unity at a lattice site and zero elsewhere [29]. There are j shells surrounding a central particle. The van der Waals theory gives the perturbation contribution to the Helmholtz energy:

$$\left(\frac{A^{\mathrm{P}}}{Nk_{\mathrm{B}}T}\right)^{\mathrm{vdW}} = \frac{1}{2T^*}\sum_j^{\mathrm{shells}} z_j u^{P*}\left(R_j^*\right), \qquad (20)$$

where z_j and $R_j^* = R_j/\sigma$ are, respectively, the number of neighboring particles in the jth shell and the reduced center-to-center distance between an arbitrarily chosen central particle and a particle in the jth shell. Because attractive forces for nonpolar molecules are short, we consider only nearest-neighbor interactions in the crystal phase. For the fcc structure, each particle has 12 nearest neighbors ($z_1 = 12$). The characteristic distance to this first shell is related to the ratio of the maximum packing fraction and the average packing fraction: $R_1/\sigma = (\eta_0/\eta)^{1/3}$. The Helmholtz energy becomes

$$\left(\frac{A^{\mathrm{P}}}{Nk_{\mathrm{B}}T}\right)^{\mathrm{vdW}} = \frac{6}{T^*}W^*, \qquad (21)$$

where the reduced perturbation energy, W^*, is defined as $W^* = u^{\mathrm{P}*}$ when $s = (\eta_0/\eta)^{1/3}$. Upon differentiating Eq. (21), the perturbation contributions to the equation of state and to the chemical potential are

$$\left(Z^{\mathrm{P}}\right)^{\mathrm{vdW}} = \frac{6\eta}{T^*}\frac{\partial W^*}{\partial\eta} \qquad (22)$$

and

$$\left(\frac{\mu^{\mathrm{P}}}{k_{\mathrm{B}}T}\right)^{\mathrm{vdW}} = \frac{6}{T^*}\left(W^* + \eta\frac{\partial W^*}{\partial\eta}\right). \qquad (23)$$

For a continuous perturbation potential, W^* and its derivatives are analytic functions.

Second-order perturbation theory for the solid

Perturbation theory, Eq. (12), is applicable to a solid phase, provided that we use a RDF and an equation of

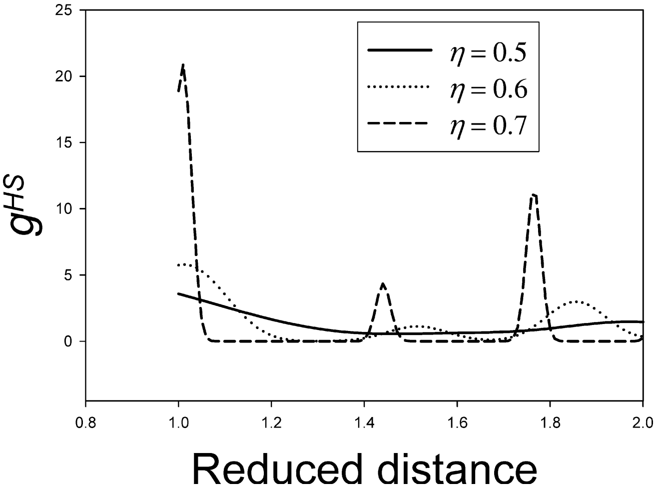

Fig. 2 Radial distribution function for a face-centered-cubic hard-sphere solid at three different packing fractions calculated from equations given by Kincaid and Weis [30]

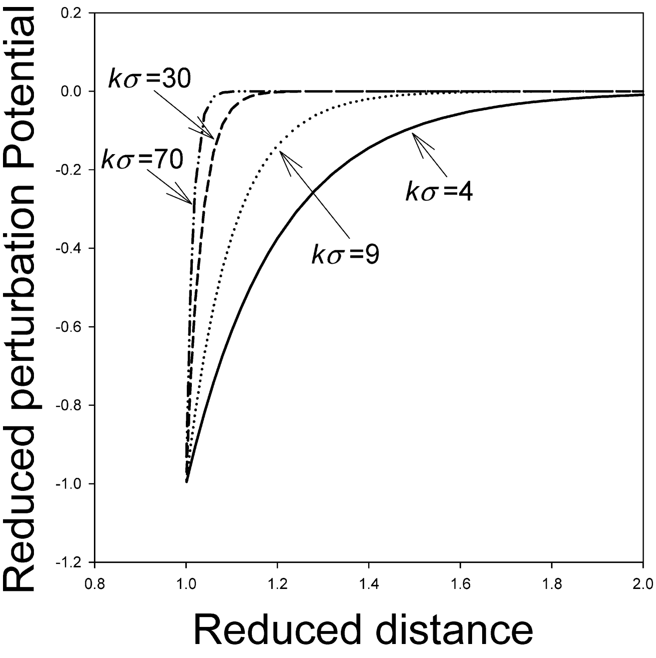

Fig. 3 Reduced perturbation (Yukawa) potential. The parameter k^{-1} is a measure of the range of attractive forces. When the parameter $k\sigma$ increases, the potential becomes shorter-ranged

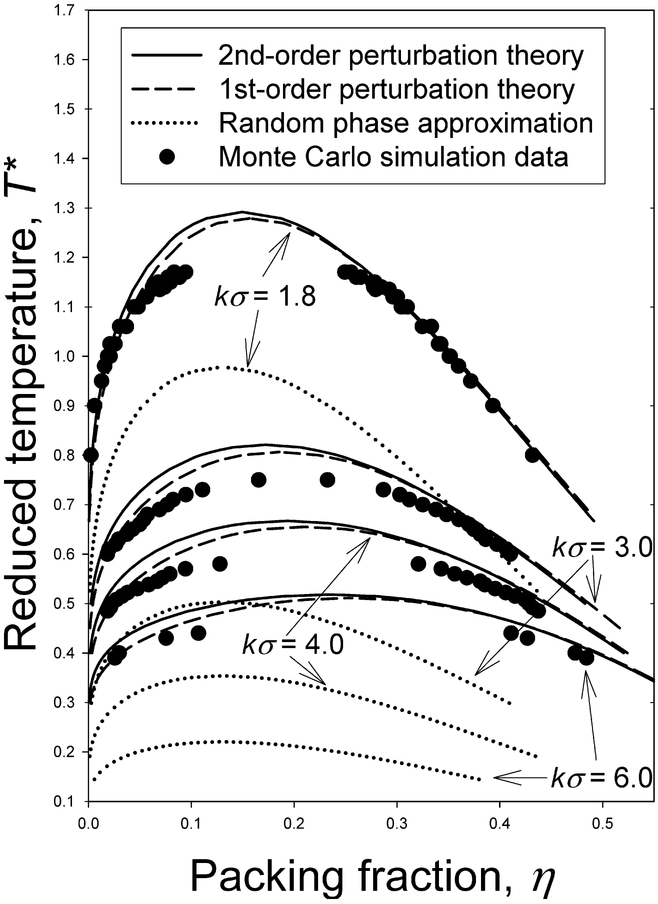

Fig. 4 Fluid–fluid phase equilibria calculated from first-order or second-order perturbation theory and from the random-phase approximation. The *points* are Monte Carlo simulation data of Shukla [16]

state for the solid-phase reference system. Because our RDF is for the fcc structure, our Barker–Henderson perturbation theory for a solid is also limited to fcc crystals. Equation (18) provides the reference equation of state for a fcc crystal system and for evaluating $\left(\frac{\partial(p/k_{\mathrm{B}}T)}{\partial\rho}\right)^{\mathrm{HS}}$. The residual perturbation contributions to the Helmholtz energy, to the equation of state, and to the chemical potential are

$$\left(\frac{A^{\mathrm{P}}}{Nk_{\mathrm{B}}T}\right)^{\mathrm{BH}} = \frac{12\eta\mathbf{I}_1}{T^*} - \frac{6\eta\left[1-(\eta/\eta_0)^{1/3}\right]^2\left(\mathbf{I}_2+\eta\frac{\partial\mathbf{I}_2}{\partial\eta}\right)}{\left[1-\frac{2}{3}(\eta/\eta_0)^{1/3}\right]}\frac{1}{(T^*)^2}, \tag{24}$$

$$\left(Z^{\mathrm{P}}\right)^{\mathrm{BH}} = \frac{12\eta}{T^*}\left(\mathbf{I}_1+\eta\frac{\partial\mathbf{I}_1}{\partial\eta}\right) - \frac{6\eta\left[1-(\eta/\eta_0)^{1/3}\right]^2\left(\mathbf{I}_2+3\eta\frac{\partial\mathbf{I}_2}{\partial\eta}+\eta^2\frac{\partial^2\mathbf{I}_2}{\partial\eta^2}\right)}{\left[1-\frac{2}{3}(\eta/\eta_0)^{1/3}\right]}\frac{1}{(T^*)^2} + \frac{12\eta(\eta/\eta_0)^{1/3}\left[1-(\eta/\eta_0)^{1/3}\right]\left[2-(\eta/\eta_0)^{1/3}\right]\left(\mathbf{I}_2+\eta\frac{\partial\mathbf{I}_2}{\partial\eta}\right)}{9\left[1-\frac{2}{3}(\eta/\eta_0)^{1/3}\right]^2}\frac{1}{(T^*)^2}, \tag{25}$$

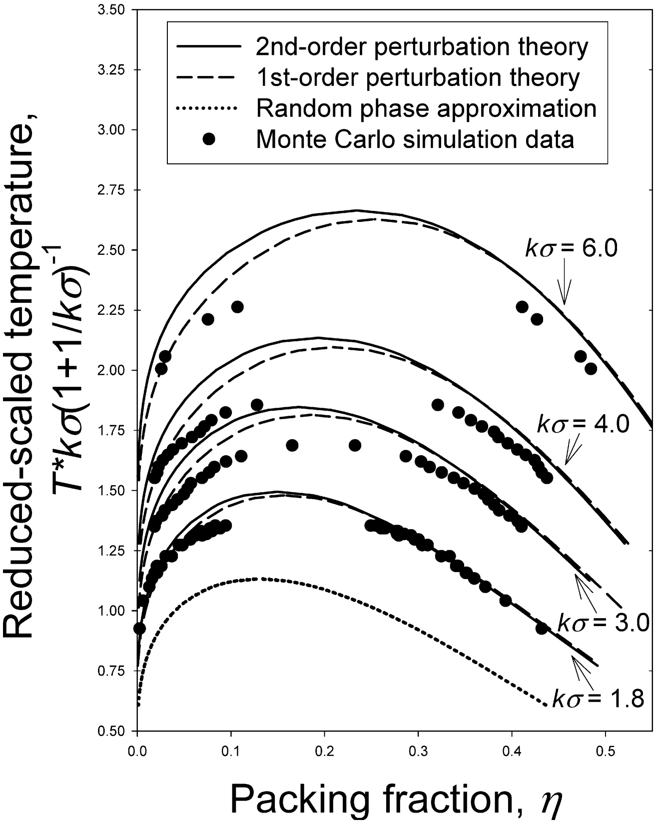

Fig. 5 Corresponding states for fluid–fluid phase equilibria based on the Yukawa potential. The results from the random-phase approximation are independent of $k\sigma$. The *points* are Monte Carlo simulation data of Shukla [16]

and

$$\left(\frac{\mu^{\mathrm{P}}}{k_{\mathrm{B}}T}\right)^{\mathrm{BH}} = \frac{12\eta}{T^*}\left(2\mathbf{I}_1+\eta\frac{\partial \mathbf{I}_1}{\partial\eta}\right) - \frac{6\eta\left[1-(\eta/\eta_0)^{1/3}\right]^2\left(2\mathbf{I}_2+4\eta\frac{\partial \mathbf{I}_2}{\partial\eta}+\eta^2\frac{\partial^2 \mathbf{I}_2}{\partial\eta^2}\right)}{\left[1-\frac{2}{3}(\eta/\eta_0)^{1/3}\right]}\frac{1}{(T^*)^2} + \frac{12\eta(\eta/\eta_0)^{1/3}\left[1-(\eta/\eta_0)^{1/3}\right]\left[2-(\eta/\eta_0)^{1/3}\right]\left(\mathbf{I}_2+\eta\frac{\partial \mathbf{I}_2}{\partial\eta}\right)}{9\left[1-\frac{2}{3}(\eta/\eta_0)^{1/3}\right]^2}\frac{1}{(T^*)^2}, \tag{26}$$

where η_0 is the maximum packing fraction, equal to $\eta_0=(\pi/6)\sqrt{2}$ for fcc crystals. The integrals $\mathbf{I}_1$, $\mathbf{I}_2$, $\frac{\partial \mathbf{I}_1}{\partial\eta}$, $\frac{\partial \mathbf{I}_2}{\partial\eta}$, and $\frac{\partial^2 \mathbf{I}_2}{\partial\eta^2}$ are similar to those of Eqs. (16), but with the RDF for a fcc crystal. Based on equations from Kincaid and Weis [30], Fig. 2 shows the RDF for a hard-sphere fcc solid as a function of reduced distance. When the packing fraction rises, the system becomes more structured, increasing the probability of finding a molecule in a lattice position around a central molecule.

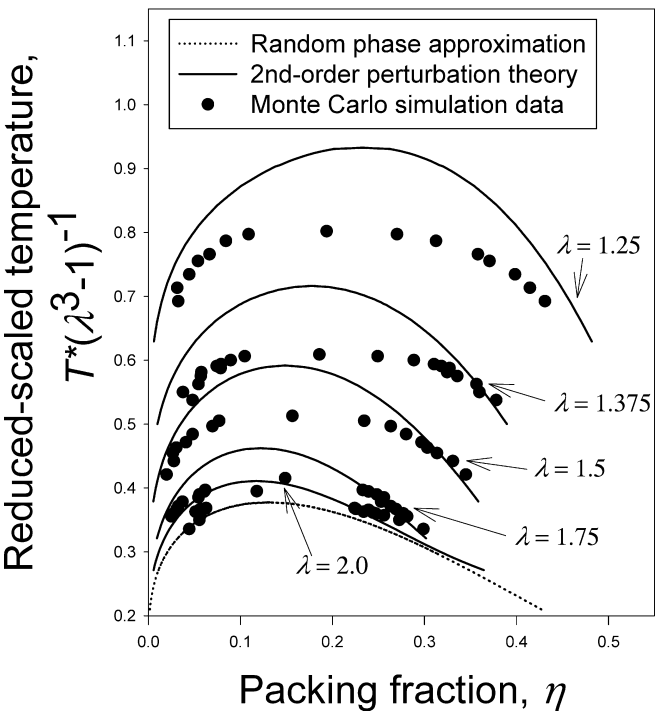

Fig. 6 Corresponding states for fluid–fluid phase equilibria based on the square-well potential. The results from the random-phase approximation are independent of λ. The *points* are Monte Carlo simulation data of Vega et al. [32]

Calculation of phase diagrams

To illustrate the applicability of the equations presented here, some phase diagrams were calculated using first-order or second-order Barker–Henderson perturbation theory, either for a fluid or for a fcc crystal; or using the RPA for the fluid and the van der Waals theory for the solid. Phase envelopes for fluid–fluid and solid–solid coexistence are obtained by using the conventional Maxwell equal-area rule. The phase equilibrium conditions are confirmed by comparing the chemical potentials of both phases at the same temperature and pressure; if the calculations are correct, these chemical potentials must be identical. Critical points are calculated using the classical conditions: $(\partial p/\partial\eta)_{T=T_c}=0$ and $\left(\partial^2 p/\partial\eta^2\right)_{T=T_c}=0$. Phase envelopes for fluid–solid equilibria are obtained using Eqs. (4) and (5).

Potential of mean force

Two particles (or molecules), represented by hard spheres with diameter σ, interact through an attractive Yukawa potential. The reduced perturbation potential $u^{\mathrm{P}*}$ is

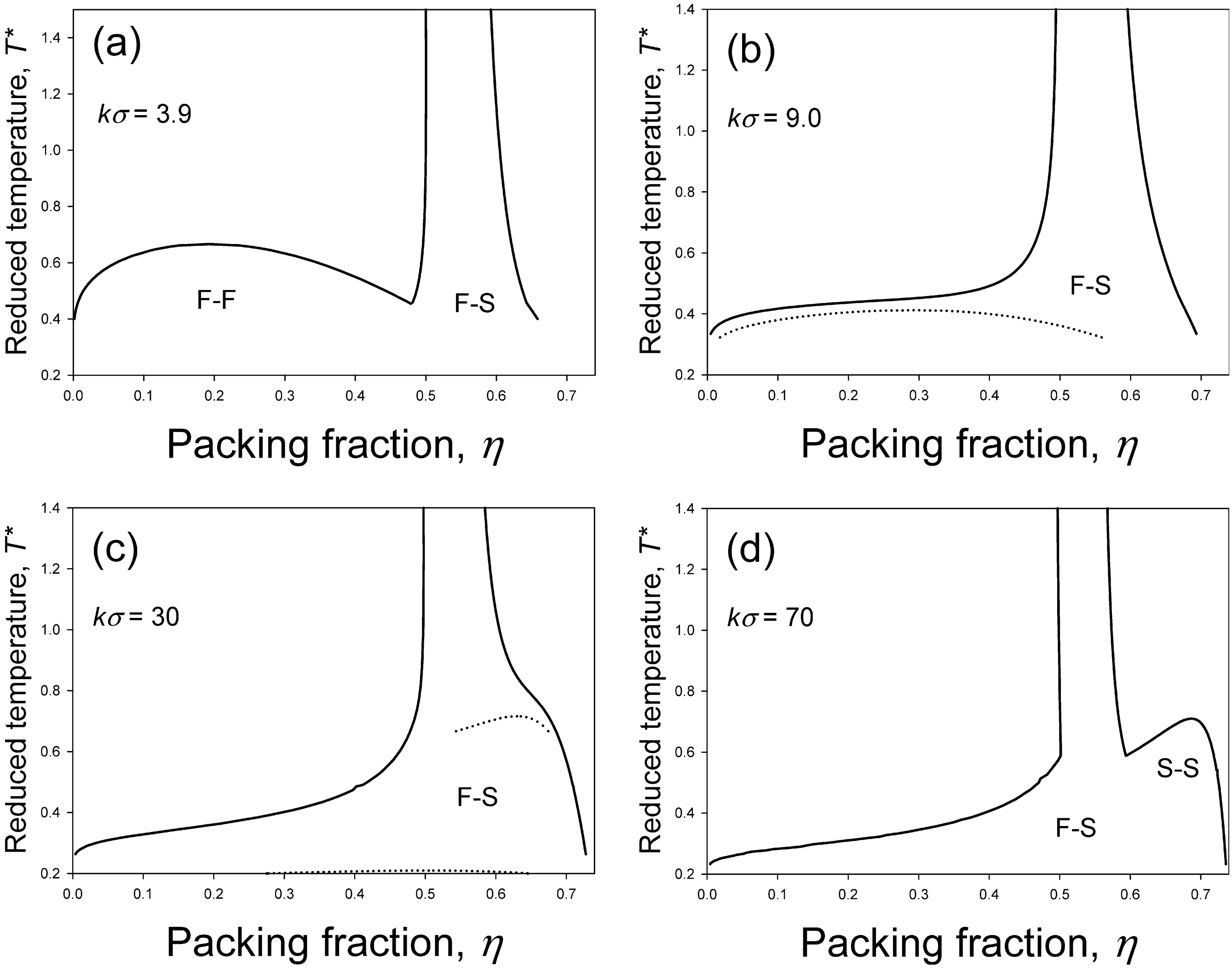

Fig. 7 Phase diagrams calculated from second-order perturbation theory based on the Yukawa potential with different ranges of attraction: **a** $k\sigma = 3.9$, **b** $k\sigma = 9$, **c** $k\sigma = 30$, and **d** $k\sigma = 70$. *Full lines* represent fluid–fluid (*F–F*), fluid–solid (*F–S*), and solid–solid (*S–S*) stable transitions. Metastable transitions are represented by *dotted lines*. The metastable fluid–fluid transition for $k\sigma = 70$ does not appear because its critical-point temperature is smaller than 0.2

$$u^{\mathrm{P}*} = \frac{u^{\mathrm{P}}}{\varepsilon} = -\frac{1}{s}\exp\left[k\sigma(1-s)\right], \qquad (27)$$

where ε and k^{-1} are parameters giving, respectively, the magnitude of the attraction and the screening length that provides a measure of the range of attractive forces. Figure 3 shows how the range of attraction rises as $k\sigma$ falls.

The Yukawa perturbation potential gives the integral that appears in the RPA:

$$\int_{1}^{\infty} u^{\mathrm{P}*} s^2 \mathrm{d}s = -\left(\frac{1}{k\sigma} + \frac{1}{(k\sigma)^2}\right). \qquad (28)$$

To calculate the Helmholtz perturbation energy for a solid, by substituting $s = (\eta_0/\eta)^{1/3}$ into Eq. (27), the Yukawa potential gives W^* and its derivative that appears in the van der Waals theory for a solid:

$$W^* = -(\eta/\eta_0)^{1/3}\exp\left\{k\sigma\left[1-(\eta_0/\eta)^{1/3}\right]\right\} \qquad (29)$$

and

$$\eta\frac{\partial W^*}{\partial\eta} = -\frac{1}{3}\left[k\sigma + (\eta/\eta_0)^{1/3}\right]\exp\left\{k\sigma\left[1-(\eta_0/\eta)^{1/3}\right]\right\}. \qquad (30)$$

To calculate the compressibility factor and chemical potential using Barker–Henderson perturbation theory, numerical integration is used for finding the integrals represented by Eq. (16); those in Eqs. (13), (14), and (15) are for the fluid and those in Eqs. (24), (25), and (26) are for the solid. We used analytic equations for the RDFs: the Chang and Sandler [27] RDF for a hard-sphere fluid and the Kincaid and Weis [30] RDF for a hard-sphere fcc crystal. Both RDFs and their first-order and second-order derivatives are real analytic expressions. The integrals $\mathbf{I}_1$, $\mathbf{I}_2$, $\frac{\partial \mathbf{I}_1}{\partial \eta}$, $\frac{\partial \mathbf{I}_2}{\partial \eta}$, and $\frac{\partial^2 \mathbf{I}_2}{\partial \eta^2}$ were calculated numerically using the Romberg integration method [31]. In these integrals, $s_{\max}$ represents the cutoff distance, i.e., the maximum distance for evaluating these integrals. Owing to the short-range forces of attraction of interest here, $s_{\max}$ for the fluid was set at 2.0. For the fcc crystal phase, the integrals were calculated using the same numerical method for a maximum of five shells surrounding a central particle in the fcc crystal lattice [30].

Results

A fluid–fluid phase diagram using the Yukawa potential is shown in Fig. 4 for several values of $k\sigma$ (1.8, 3.0, 4.0, and 6.0). As $k\sigma$ rises, the range of attraction falls. For comparison, results are shown for first-order or second-order Barker–Henderson perturbation theories and for the RPA. Figure 4 also presents Monte Carlo simulation data of Shukla [16]. The results are very similar for first-order and second-order perturbation theories but differ markedly from those for the RPA. As expected for a classical theory, first-order and second-order perturbation theories overpredict the critical temperature. Figure 4 also shows that the RPA underpredicts the critical temperature. The results are worst for higher values of $k\sigma$, i.e., for short-ranged potentials, the RPA is very poor. The RPA is expected to become more accurate for a long-ranged potential because it is exact for systems with infinitely weak and infinitely long range attraction.

Differences between the calculated results become more evident when a modified reduced temperature is defined. A reduced-scaled temperature is obtained by dividing the reduced temperature $T^* = k_B T/\varepsilon$ by a term proportional to the integral $\int_1^\infty u^{P*} s^2 ds$. From Eq. (28), the reduced-scaled temperature based on the Yukawa potential is $(T^* k\sigma)(1 + 1/k\sigma)^{-1}$. For this temperature scale, the RPA obeys corresponding states, i.e., the phase envelopes for different values of $k\sigma$ collapse to one curve. Fluid–fluid phase diagrams obtained using the first-order or second-order perturbation theories and the RPA are shown in Fig. 5. Neither Monte Carlo simulations nor first-order and second-order perturbation theories obey this form of corresponding states.

Similar calculations are presented in Fig. 6 for the square-well potential. For this case, the reduced-scaled temperature is $T^*(\lambda^3 - 1)^{-1}$, where λ is related to the width of the potential through $\lambda\sigma = (\text{width} + \sigma)$. For Figs. 5 and 6, the RPA improves for long-range potentials. Figures 5 and 6 indicate that for short-ranged potentials, the structural information included in the RDF is important for reliable predictions of phase diagrams; in other words, for short-ranged potentials, the simple van der Waals perturbation (where g^{HS} is independent of density and temperature) is poor.

Using second-order perturbation theory for both solid and fluid phases, we calculated complete phase diagrams based on the Yukawa potential for different values of $k\sigma$. The results are presented in Fig. 7, in a sequence where we increase the range of the potential. Coexistence of stable fluid–fluid and solid–fluid phases is shown in Fig. 7a. Therefore, for a long-range potential ($k\sigma = 3.9$), the second-order perturbation theory shows that there exists a fluid–fluid critical point and a fluid–fluid–solid triple-point temperature. For short-range potentials ($k\sigma = 9$ and 30), fluid–solid equilibria are stable but fluid–fluid equilibria are not. Both fluid–fluid and solid-solid equilibria are metastable, represented by

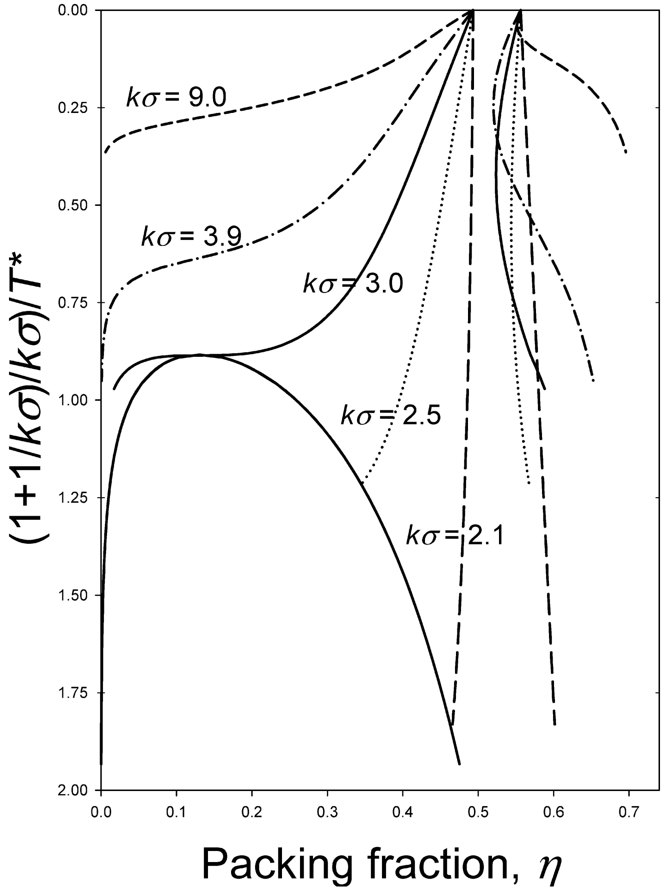

Fig. 8 Phase diagrams calculated from the random-phase approximation based on the Yukawa potential with different ranges of attraction ($k\sigma = 2.1$, 2.5, 3.0, 3.9, and 9.0). Because corresponding states hold when the temperature is reduced as shown, *one full line* represents all fluid–fluid equilibria. A *pair of lines* represents fluid–solid transitions for a specific value of $k\sigma$. A *pair of long-dashed lines* represents fluid–solid equilibria for $k\sigma = 2.1$; *dotted lines* for $k\sigma = 2.5$; *full lines* for $k\sigma = 3.0$; *dot-dashed lines* for $k\sigma = 3.9$; and *short-dashed lines* for $k\sigma = 9.0$

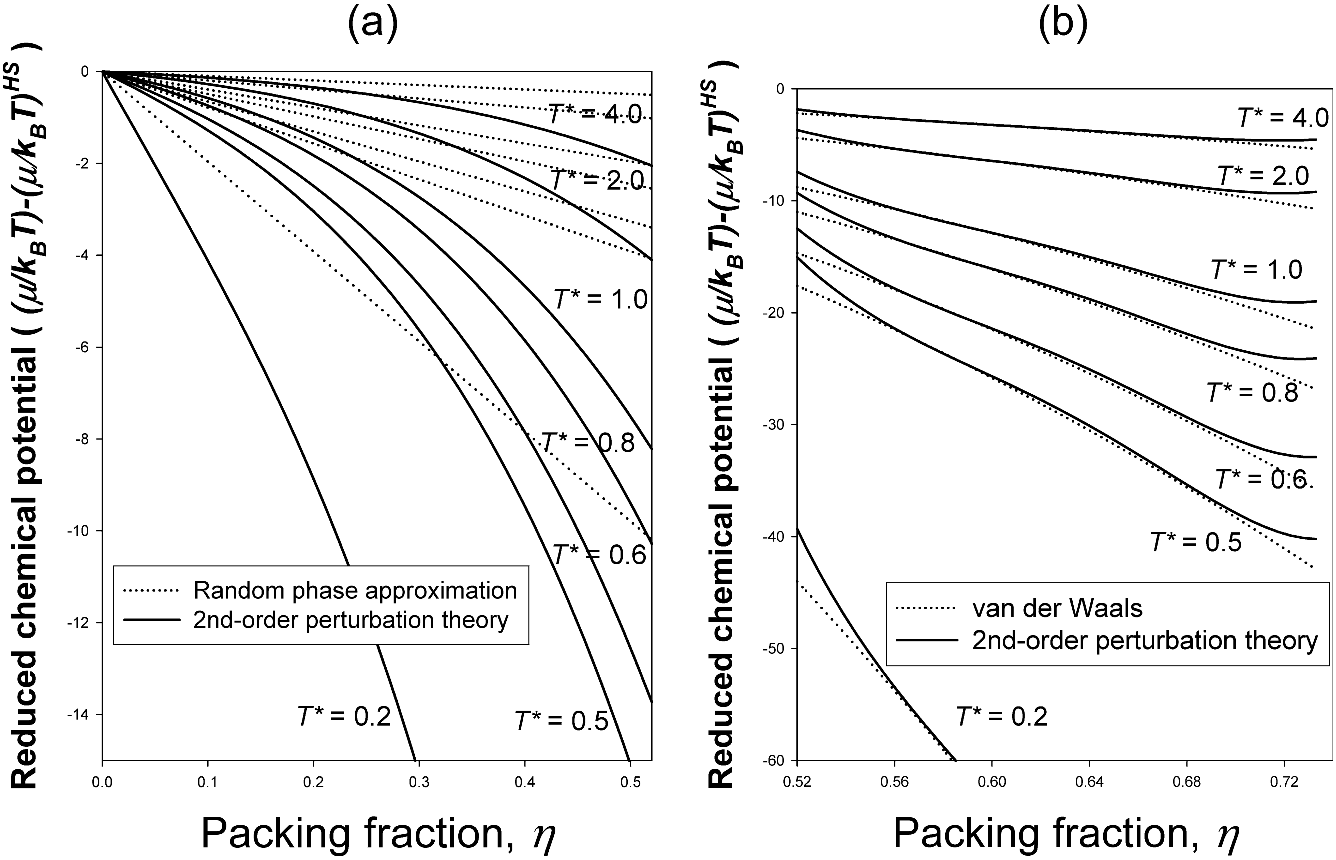

Fig. 9a,b Comparison of the chemical potential calculated with different models for fluid and solid phases when the Yukawa potential ($k\sigma = 7$) is used. **a** Comparison of the random-phase approximation with second-order perturbation theory for the fluid phase. **b** Comparison of the van der Waals theory with second-order perturbation theory for the solid phase

dotted lines in Fig. 7b and c, respectively. For a very short-ranged potential ($k\sigma = 70$), the isostructural (fcc–fcc) solid–solid transition is stable (Fig. 7d). For $k\sigma = 70$, we see a solid–solid critical point and a fluid–solid–solid triple-point temperature. These results are similar to those obtained by Monte Carlo simulation [14].

Using the RPA for the fluid phase and the van der Waals theory for a fcc crystal phase, we obtained phase diagrams based on the Yukawa potential. The results for different values of the screening length parameter are shown in Fig. 8. To show results for higher temperatures, Fig. 8 is a plot of the inverse reduced-scaled temperature versus packing fraction. When $T^* \rightarrow \infty$, the hard-sphere solid–fluid phase transition is independent of screening length and in very good agreement with results obtained by Wu. These models (RPA and van der Waals) predict that the fluid–fluid phase transition is stable for $k\sigma < 3$. For shorter-range potentials, only solid–fluid equilibria are stable. Because structural information is included in the van der Waals theory for the solid, the solid–fluid phase transition does not obey corresponding states.

Figure 9 shows a comparison between the RPA and second-order Barker–Henderson perturbation theory for the fluid (Fig. 9a), and between van der Waals and second-order Barker–Henderson perturbation theories applied to fcc crystals (Fig. 9b), for $k\sigma = 7$. This comparison shows that the chemical potentials calculated by the RPA are significantly different from those calculated by second-order perturbation theory. For the solid phase, both theories, van der Waals and second-order perturbation, give similar chemical potentials, at least for intermediate densities. The deviation shown at higher densities, Fig. 9b, follows primarily from using only the first shell in van der Waals theory for a solid.

To explore the possibility of obtaining two fluid–fluid critical points, we consider a potential of mean force that has a second minimum. According to Israelachvili [33], a sum of three parts, hard-sphere contribution, double-layer (charge–charge) repulsion, and van der Waals attraction, can give a double-minimum potential as shown in Fig. 10. Between the two minima, the potential presents a peak, i.e., an energy barrier. As pointed out by Israelachvili [33], the energy barrier and the second minimum in the

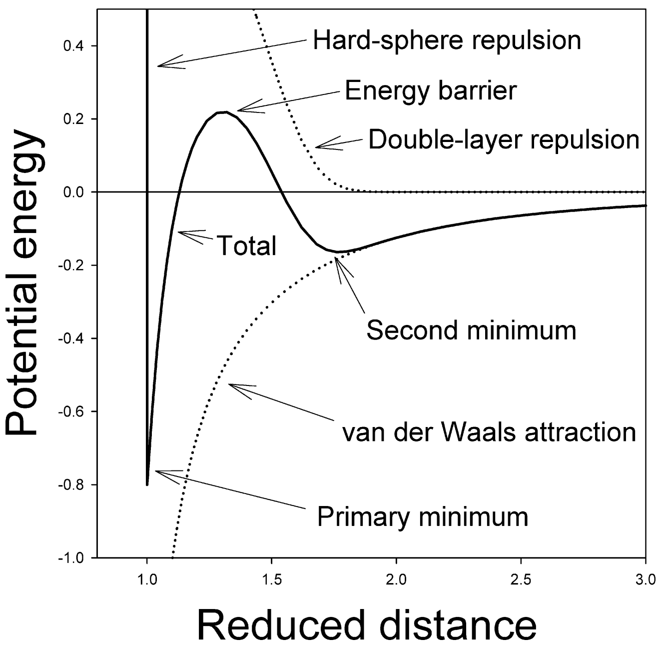

Fig. 10 Total perturbed hard-sphere potential energy given by a sum of hard-sphere, double-layer (charge–charge) repulsion, and van der Waals attraction contributions. The potential presents two minima and an energy barrier

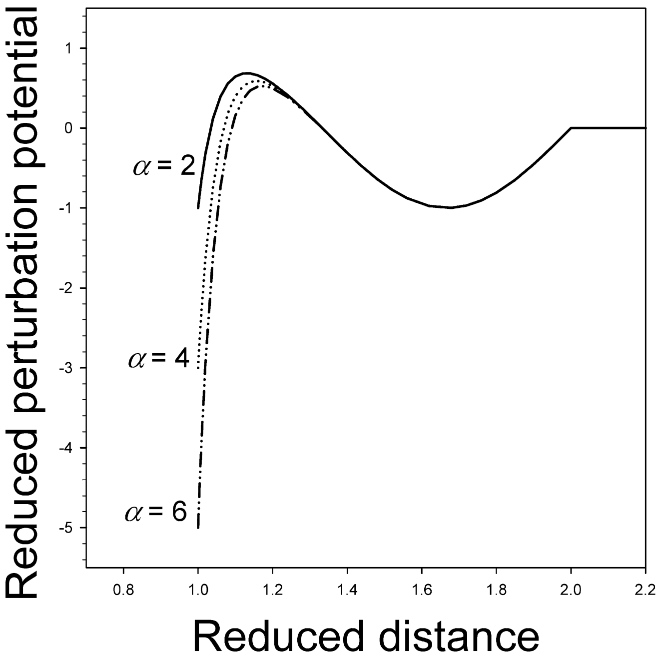

Fig. 11 Double-minimum perturbation potentials. The surface of the hard core is at $s=1$ (for $s<1$, the total potential is ∞). These potentials have two minima, one minimum (primary minimum) at the hard core ($s=1$) and the other (second minimum) at about $s=1.67$. The depth of the primary minimum is equal to $-\varepsilon(\alpha-1)$ and the depth of the second minimum is $-\varepsilon$

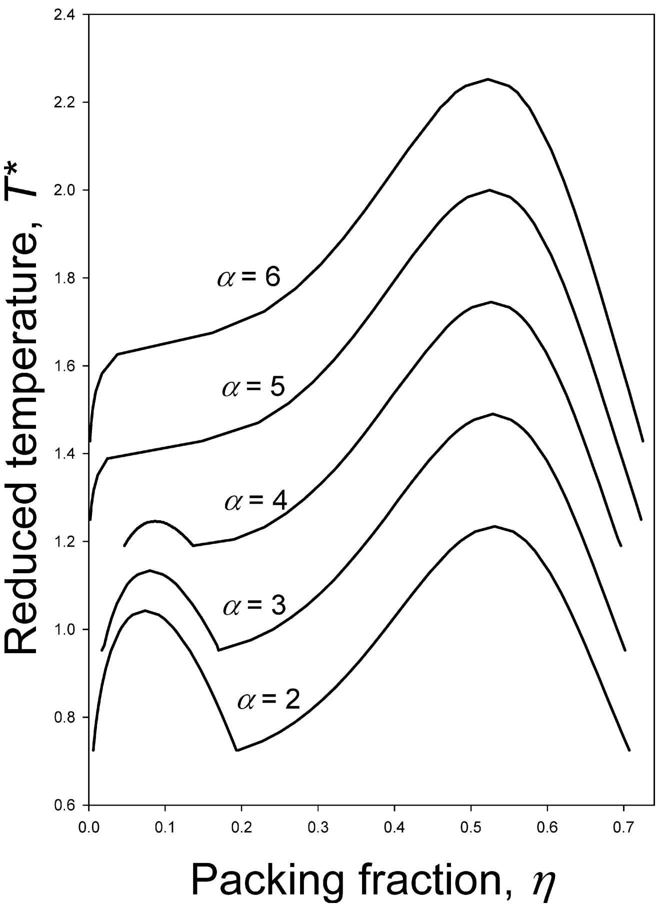

Fig. 12 Fluid–fluid phase equilibria calculated from second-order perturbation theory for different values of α. The phase diagram shows two regions of fluid–fluid coexistence, one at low packing fraction and the other at high packing fraction. When α increases, low-density fluid–fluid coexistence disappears

potential are directly related to the rate of colloid coagulation. We now consider the phase diagrams for these potentials. For the double-minimum potential we use a sum of a Yukawa potential and a cosine function:

$$\begin{aligned} u^{P*} &= -(\alpha/s)\exp[20(1-s)] + \cos[1.5\pi(1-s)] \\ &\qquad \text{for } 1\leqslant s\leqslant 2, \qquad (31) \\ u^{P*} &= 0 \quad \text{for } s>2, \end{aligned}$$

where $u^{P*}=u^{P}/\varepsilon$ is the reduced perturbation potential and $\alpha-1$ is the relative depth of the primary minimum. The second minimum is obtained from a simple cosine expression. The first minimum is at $s=1$. When the depth of the second minimum is $-\varepsilon$, the depth of the first minimum is $-\varepsilon(\alpha-1)$.

As shown in Fig. 11, upon increasing α, the attraction corresponding to the primary minimum increases and the height of the repulsion barrier decreases.

Using second-order Barker–Henderson perturbation theory, fluid–fluid phase diagrams are presented in

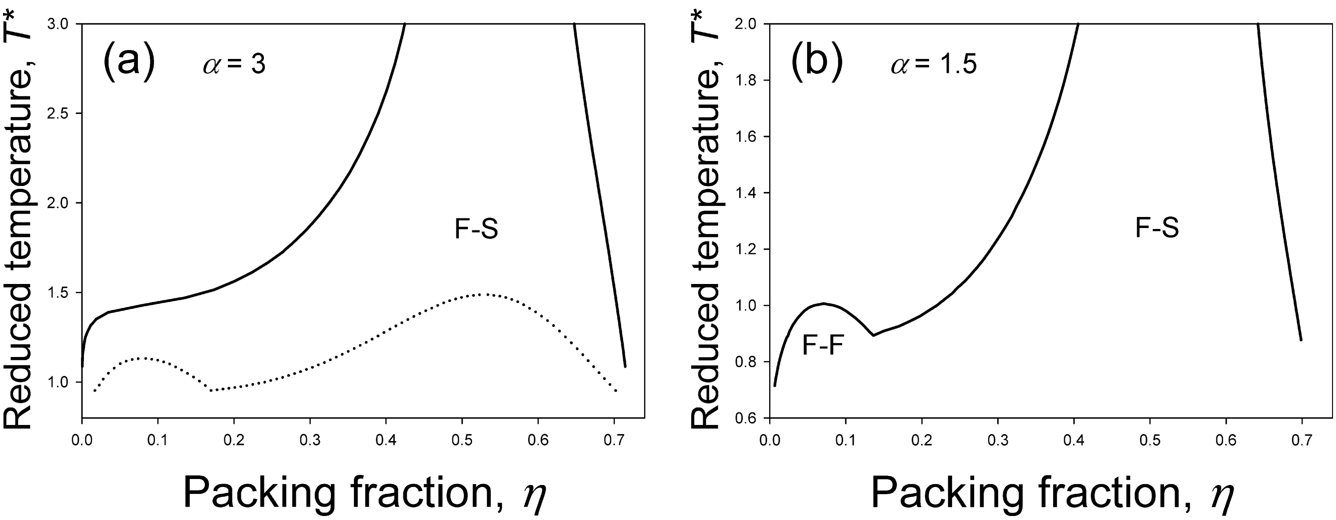

Fig. 13 Fluid–fluid and fluid–solid phase diagrams calculated from second-order perturbation theory based on double-minimum potentials: **a** $\alpha = 3$ and **b** $\alpha = 1.5$. Stable regions are represented by *full lines* and metastable regions by *dotted lines*

Fig. 12 for several α. All the results are expressed in terms of reduced temperature $T^* = k_B T/\varepsilon$. For $\alpha = 2$, 3, and 4, we obtain two critical points, one at low packing fraction, near $\eta = 0.09$, and the other at high packing fraction, near $\eta = 0.51$. When α increases, the extent of low-density fluid–fluid coexistence decreases and the low-density fluid–fluid critical point moves slightly toward higher packing fractions. The high-density fluid–fluid coexistence is less sensitive to α. These systems also give a triple-point temperature where three fluid phases are in equilibrium, i.e., we obtain a fluid–fluid–fluid coexistence temperature. For higher values of α, for example $\alpha = 5$ or 6, shown in Fig. 12, the low-density fluid–fluid transition disappears and the system gives only one critical point. Although phase diagrams based on Eq. (31) give topologically rich phase behavior, for the range of parameters studied here ($2 \le \alpha \le 6$), the solid–fluid transition is stabler than the fluid–fluid transition. As an example for $\alpha = 3$, Fig. 13a presents a phase diagram including the solid–fluid transition that is stable and a fluid–fluid coexistence that is metastable. However, for a smaller attraction corresponding to the primary minimum, $\alpha = 1.5$, the phase diagram presents a stable low-density fluid–fluid region shown in Fig. 13b.

Conclusion

We have given an overview of analytic calculation of phase diagrams encountered in aqueous solutions of colloids or globular proteins. While such phase diagrams have been calculated previously, mostly by molecular simulations, our calculations are entirely analytic. We have applied standard molecular thermodynamics to generate phase diagrams for solution of colloids and globular proteins. The particle–particle interaction is given by a perturbed hard-sphere potential of mean force where the perturbation is given by the Yukawa potential. Second-order Barker–Henderson perturbation theory, applied to both fluid and solid phases, gives a complete phase diagram, including fluid–fluid, fluid–solid, and solid–solid equilibria. Comparison with molecular-simulations is good. However, when the same calculations are performed using the much-simplified RPA to describe the fluid phase and the simple van der Waals model for a fcc crystal, the results do not agree well with those from molecular simulation. We have also considered the possible appearance of two fluid–fluid critical points. Using second-order perturbation theory and a double-minimum potential, we have shown the existence of both low-density and high-density fluid–fluid phase transitions. However, the higher-density transition is metastable.

The calculation procedures described here may be useful for guiding and interpreting experimental work and for design of separation operations.

Acknowledgements For financial support, F.W.T. is grateful to CAPES/Brazil (Ministério da Educação) for grants BEX 0621/02-1 and both authors are grateful to the Office for Basic Sciences of the U.S. Department of Energy and to the National Science Foundation. The authors also thank J.Z. Wu (University of California, Riverside, CA) for helpful comments and for sending us unpublished material.

References

1. Evans DF, Wennerström H (1999) The colloidal domain: where physics, chemistry, biology, and technology meet, 2nd edn. Wiley, New York
2. Anderson VJ, Lekkerkerker HNW (2002) Nature 416:811–815
3. Debenedetti PG (1986) Metastable liquids: concepts and principles. Princeton University Press, Princeton, NJ
4. Renth F, Poon WCK, Evans RML (2001) Phys Rev E 64:031402
5. Evans RML, Poon WCK, Renth F (2001) Phys Rev E 64:031403
6. Gast AP, Hall CK, Russel WG (1983) J Colloid Interface Sci 96:251
7. Mahadevan H, Hall CK (1990) AIChE J 36:1517–1528
8. Fornasiero F, Ulrich J, Prausnitz JM (1999) Chem Eng Process 38:463–475
9. Wu JZ, Prausnitz JM (2002) Fluid Phase Equilib 194–197:689–700
10. Tejero CF, Daanoun A, Lekkerkerker HNW, Baus M (1995) Phys Rev E 51:558
11. Daanoun A, Tejero CF, Baus M (1994) Phys Rev E 50:2913
12. Hagen MHJ, Frenkel D (1994) J Chem Phys 101:4093
13. Tavares FW, Sandler SI (1997) AIChE J 43:218–231
14. Dijkstra M (2002) Phys Rev E 66:021402
15. Bolhuis P, Hagen M, Frenkel D (1994) Phys Rev E 50:4880
16. Shukla KP (2000) J Chem Phys 112:10358
17. Mishima O (2000) Phys Rev Lett 85:334
18. Katayama Y, Mizutani T, Utsumi W, Shimomura O, Yamakata M, Funakoshi K (2000) Nature 403:170
19. Lacks DL (2000) Phys Rev Lett 84:4629
20. van Thiel M, Ree FH (1993) Phys Rev B 48:3591
21. Hemmer PC, Velasco E, Mederos L, Navascues G, Stell G (2001) J Chem Phys 114:2268–2265
22. Franzese G, Malescio G, Skibinsky A, Buldyrev S, Stanley HE (2001) Nature 409:692
23. Malescio G, Franzese G, Pellicane G, Skibinsky A, Buldyrev SV, Stanley HE (2002) J Phys Condens Matter 14:2193–2200
24. Velasco E, Mederos L, Navascues G (1998) Langmuir 14:5652–5655
25. McQuarrie DA (1973) Statistical mechanics. Harper Collins, New York
26. Boublik T, Nezbeda I, Hlavaty K (1980) Statistical thermodynamics of simple liquids and their mixtures. Elsevier, New York
27. Chang J, Sandler SI (1994) Mol Phys 81:735
28. Hoover WG, Ree FH (1968) J Chem Phys 49:3609
29. Daanoun A, Tejero CF, Baus M (1994) Physi Rev E 50:2913–2924
30. Kincaid JM, Weis JJ (1977) Mol Phys 34:931
31. Press WH, Teukolsky SA, Vetterling WT, Flami BP (192) Numerical recipes in FORTRAN: the art of scientific computing. Cambridge University Press, Cambridge, UK
32. Vega L, de Miguel E, Rull LF, Jackson G, McLure I (1992) J Chem Phys 96:2296
33. Israelachvili J (1991) Intermolecular and surface forces, 2nd edn. Academic, London